https://doi.org/10.5194/egusphere-2025-4248
Preprint. Discussion started: 12 September 2025

A dual-frequency (W-band and G-band) radar optimal estimation framework to retrieve drizzle properties more accurately

Juan M. Socuellamos, Matthew D. Lebsock, Raquel Rodriguez Monje, Marcin J. Kurowski, Derek J. Posselt, and Robert M. Beauchamp

Jet Propulsion Laboratory, California Institute of Technology, Pasadena, CA 91109, USA

Correspondence to: Matthew D. Lebsock (matthew.d.lebsock@jpl.nasa.gov)

Abstract. High-resolution cloud radar observations are generated from a large eddy simulation of drizzling marine stratocumulus. These observations are then used to investigate dual-frequency measurements combining W-band (94 GHz) and G-band (239 GHz), a pairing that offers unique sensitivity to early-stage drizzle and small liquid water paths by exploiting the differential backscatter and extinction signatures of hydrometeors. An optimal estimation framework is implemented to retrieve key drizzle microphysical properties from the simulated observations. We demonstrate that the synergies of a nadir-looking W-band and G-band radar system can result in more than one order of magnitude reduction in the uncertainty of the estimated drizzle mass mixing ratio, number concentration, and mass-weighted mean diameter compared to W-band only observations. The methodology can be applied to W-band and G-band airborne observations to improve drizzle estimation. Furthermore, we show that these reductions in uncertainty can be attainable from a spaceborne platform with mission architecture and radar parameters realizable with current technology.

1 Introduction

Atmospheric radars are the primary tool to study the internal structure of clouds and precipitation because of their ability to penetrate cloud layers and provide fine range resolution. Since smaller hydrometeors scatter radar signals weakly, high-sensitivity radars are required to accurately retrieve cloud and light-precipitation properties. This is particularly true for stratocumulus, which are largely composed of small cloud and drizzle droplets (mean diameters < 500 μm) and typically low water content, making them especially difficult to detect and characterize. Moreover, hydrometeors within this size range play a critical role in several processes, including cloud-climate feedback (Mülmenstädt et al., 2021), aerosol effects on cloud albedo (Jing and Suzuki, 2018), and microphysical processes in ice-liquid conversion (Zhang et al., 2019).

A defining characteristic of stratocumulus is their tendency to drizzle, often accompanied by distinct differences in cloud structure between non-precipitating and precipitating conditions (Muhlbauer et al., 2014). Ka-band (35 GHz) and W-band (94 GHz) radars from ground-based or airborne platforms are frequently used to observe these transitions. However, distinguishing precipitation from cloud remains challenging due to uncertainty in the reflectivity value chosen as a threshold to separate both modes, especially when higher-order Doppler moments are not available (Zhu et al., 2022). From space, only two W-band radars have operated with the sensitivity needed to detect the onset of drizzle: NASA's CloudSat (Stephens et al.,

https://doi.org/10.5194/egusphere-2025-4248
Preprint. Discussion started: 12 September 2025

2008), now decommissioned, and ESA-JAXA's EarthCARE mission (Wehr et al., 2023), currently in operation and expected to continue until at least 2028. Despite the advantage of their global coverage, these satellite instruments struggle to identify precipitation onset due to non-existent or inaccurate higher-order Doppler moments, causing important discrepancies in global precipitation estimates (Liu et al., 2008; Tansey et al., 2022).

Incorporating higher-frequency millimeter-wave radars offers a pathway to improve the sensitivity and accuracy of drizzle retrievals. Specifically, by combining concurrent radar measurements at two or more millimeter-wave frequencies, the differential scattering and absorption signals can be exploited to determine parameters of the drop size distribution (Lhermitte, 1990; Lamer et al., 2021). As shown in the backscattering and extinction efficiencies in Fig. 1, computed using Mie electromagnetic theory assuming a spherical liquid drop at 280 K, a radar signal at G-band (239 GHz) begins to exhibit non-Rayleigh scattering effects for drop diameters as small as 100 µm. This earlier deviation from Rayleigh scattering compared to the W-band and Ka-band curves provides additional information to characterize microphysics in the range of drop sizes representative of embryonic precipitation drops and the region where cloud and precipitation coexist (Beard and Ochs, 1993). While Ka-band and W-band dual-frequency measurements are better suited to investigate rain drop size distributions, the W-band and G-band pair offers distinct benefits to study stratocumulus and drizzle formation since these clouds tend to contain relatively small mean drop diameters (< 500 µm) and low amounts of liquid water path (< 200 gm^{-2}) (O'Connor et al., 2005; O'Dell et al., 2008). A W-band and G-band radar system possesses the ability to size drizzle droplets as small as 100 µm in diameter through the differential backscattering ratio (Battaglia et al., 2014) and to quantify cloud water content as low as 0.1 gm^{-3} from differential attenuation measurements (Socuellamos et al., 2024b). Even though the unique potential of G-band weather radars has been recently demonstrated through ground-based observations (Courtier et al., 2022; Socuellamos et al., 2024a; Yurk et al., 2025), the utility of differential W-band and G-band measurements to estimate drizzle properties has yet to be adequately quantified.

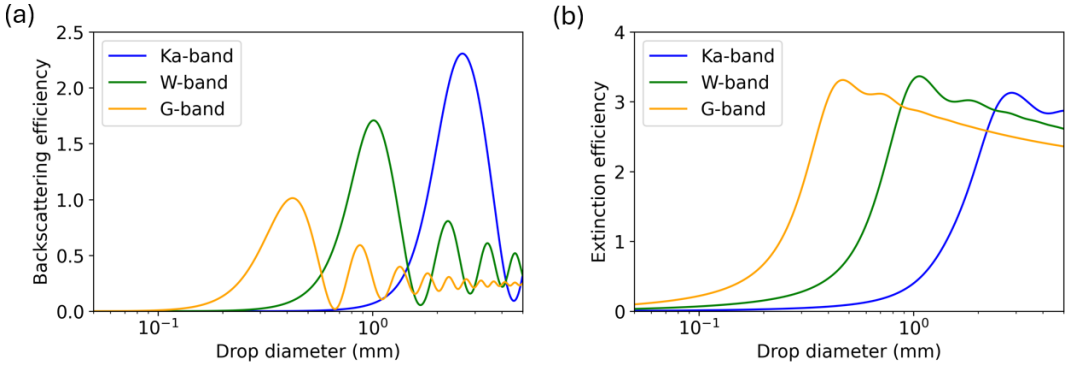

Figure 1: Single-drop backscattering (a) and extinction (b) efficiency as a function of the drop diameter at Ka-band (35 GHz), W-band (94 GHz), and G-band (239 GHz).

https://doi.org/10.5194/egusphere-2025-4248
Preprint. Discussion started: 12 September 2025

In this work, we explore the ability of W-band and G-band dual-frequency radar reflectivity measurements to constrain precipitation microphysics in stratocumulus. We simulate airborne and spaceborne W-band and G-band radar observations of drizzling boundary layer clouds from a Large Eddy Simulation (LES) model based on the VAMOS Ocean-Cloud-Atmosphere-Land Study (VOCALS; Wood et al., 2011) international field program. We then adopt and expand an optimal estimation framework, commonly used in atmospheric retrievals to estimate state variables from observations (Rodgers, 2000; Maahn et al., 2020), to include dual-frequency radar measurements. After implementing the algorithm and comparing the results between a dual-frequency W-band and G-band radar system and a W-band only radar, we demonstrate that the dual-frequency reflectivity ratio (*DFR*) and the differential path integrated attenuation (*DPIA*) impose new constraints in the optimal estimation algorithm for improved retrieval accuracy of drizzle properties of more than one order of magnitude compared to W-band only radar measurements.

2. Simulated radar observations

2.1 VOCALS LES setup

The large eddy simulation used as the nature run in this planetary boundary layer retrieval Observing System Simulation Experiment (OSSE) (Kurowski et al., 2023) was produced using the System for Atmospheric Modeling (Khairoutdinov and Randall, 2003). The modeling setup follows Brener et al. (2011), and is designed to represent marine stratocumulus characteristic of the subtropical southeast Pacific region off the coast of Peru. It is based on observations from the VOCALS Regional Experiment (Wood et al., 2011). The domain is centered around 17.5°S latitude and 79.0°W longitude, well within the VOCALS observational region known for persistent stratocumulus decks exhibiting both closed and open cell structures.

The simulation employs a bidimensional channel domain with periodic boundary conditions in both horizontal directions. The domain spans 81.92 km x 20.48 km and is discretized into 4096 x 1024 grid points, with a horizontal resolution of 20 m that allows for resolving cloud and precipitation structures in detail. The vertical grid consists of 384 stretched levels extending to around 29 km, with vertical spacing of approximately 30 m near the surface, refined to about 5 m within the cloud layer, and stretched again above. Spatially homogeneous surface fluxes are prescribed at 3 Wm^{-2} for sensible heat and 148 Wm^{-2} for latent heat. The simulation assumes the limit of free convection, with no background horizontal wind. This idealized condition was chosen to maintain the prescribed distribution of cloud droplet number concentration of 100 cm^{-3} in the polluted half of the domain and of 10 cm^{-3} in the pristine half (see Fig. 2(c)), without a large-scale advection of cloud structures between the two regions. A linear transition in terms of cloud droplet number concentration approximately 5 km wide connects the two regions. This configuration supports the coexistence of closed cells of weakly drizzling stratocumulus in the polluted region and open cells of strongly drizzling clouds in the pristine region, as shown in Fig. 2(d) and Fig. 2(e). The resulting variability in precipitation rates across the domain allows for evaluation of the retrieval algorithm over a range of stratocumulus conditions. Radiative effects are represented using the radiative transfer scheme of Iacono et al. (2008), while cloud microphysics is handled using the two-moment scheme of Morrison and Gettelman (2008). The atmospheric state is initially

https://doi.org/10.5194/egusphere-2025-4248
Preprint. Discussion started: 12 September 2025

90 homogeneous, and the simulation is integrated for 8 hours, allowing the system to evolve into a quasi-steady, heterogeneous state with various sizes of convective cells, capped by a strong temperature inversion. The resulting heterogeneity is well represented by the visible optical depth in Fig. 2(a), computed using the drop size distribution described in Sect. 2.2 and Eq. (6) at visible wavelengths, where the convective cells typically span a few kilometers across both dimensions. The transition between the polluted (optically thick) and pristine (optically thin) domains is also evident at around the 40-km mark.

95

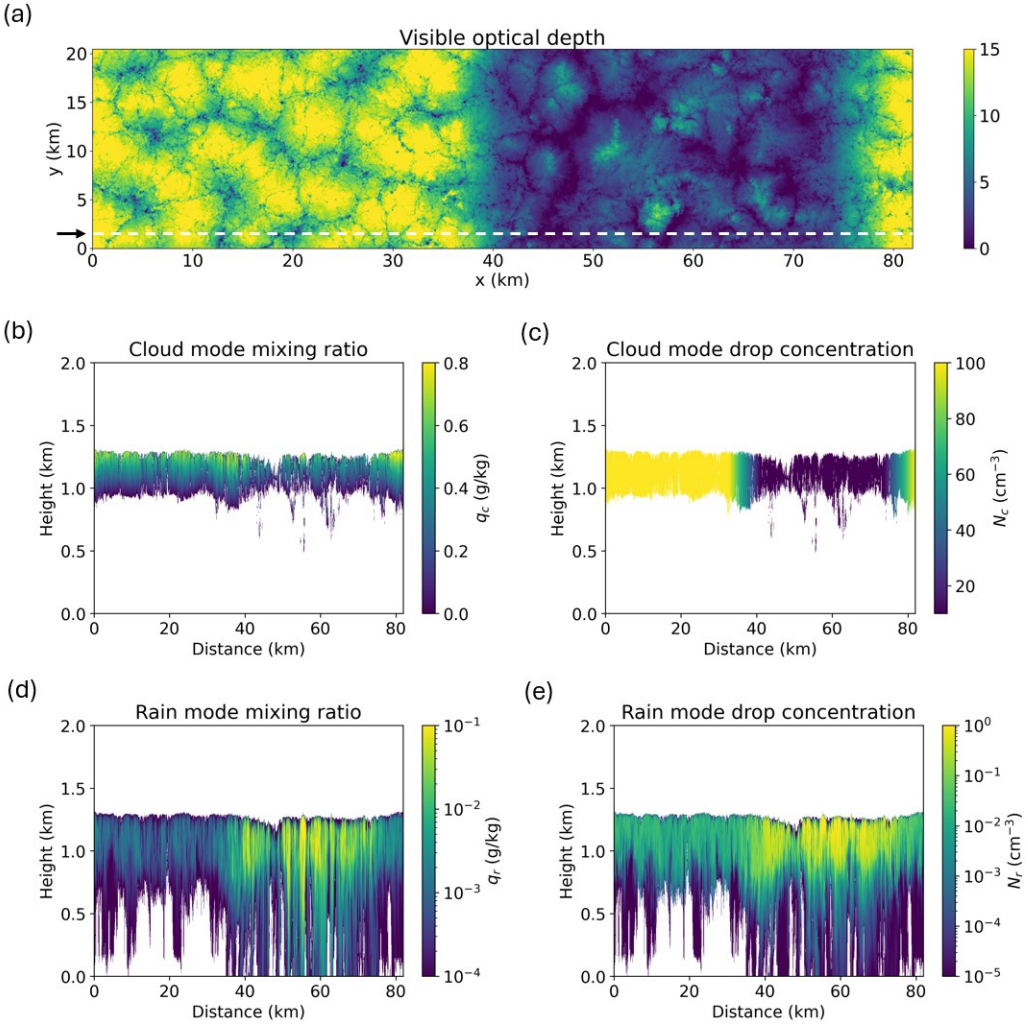

Figure 2: (a) Visible optical depth corresponding to the computed VOCALS simulations; the arrow and dashed line indicate the cross-section chosen for analysis in this work. The cloud mixing ratio (b), cloud drop concentration (c), rain mixing ratio (d), and rain drop concentration (e) are shown for such cross-section.

100

https://doi.org/10.5194/egusphere-2025-4248
Preprint. Discussion started: 12 September 2025

2.2 Simulated radar measurements

To convert the simulated cloud and rain properties presented in Sect. 2.1 into simulated radar observations, we adopted a three-parameter gamma drop size distribution (DSD) to describe the dependance of the concentration of droplets, N, on the droplet diameter, D. The gamma DSD is given by

$$N(D) = N_0 D^{\mu} e^{-\lambda D}, \tag{1}$$

with N_0, λ, and μ being the intercept, slope and shape parameters, respectively. While we acknowledge the great variability that the shape parameter may have, we assumed $\mu = 1$ to represent both cloud and rain modes. This value bridges the typical range where $\mu = 0$ is often used for rain (Abel and Boutle, 2012) and $\mu \geq 2$ for non-precipitating clouds (Miles et al., 2000). Using the cloud and rain mixing ratios, q_c and q_r, and the drop concentrations, N_c and N_r, shown in Fig. 2, we express $\lambda_{c/r}$ and $N_{0,c/r}$ as (Straka, 2011)

$$\lambda_{c/r} = \left(\frac{a_m N_{c/r} \Gamma(\mu + b_m)}{q_{c/r} \rho_a \Gamma(\mu + 1)} \right)^{\frac{1}{b_m}}, \tag{2}$$

$$N_{0,c/r} = \frac{N_{c/r} \lambda_{c/r}^{\mu+1}}{\Gamma(\mu + 1)}, \tag{3}$$

where $\Gamma(x)$ is the gamma function, ρ_a the air density and $m = a_m D^{b_m}$ the mass-diameter relationship for spherical liquid drops with $a_m = \pi\rho_w/6$, ρ_w the water density, and $b_m = 3$.

The frequency-dependent observed radar reflectivity, $Z(f)$, can be computed as the equivalent reflectivity factor, $Z_e(f)$, that is directly related to the hydrometeor backscattered power, minus the amount of energy that is lost due to hydrometeor extinction, $k_h(f)$, and absorption by atmospheric gases, $k_g(f)$, in the radar signal's two-way path to the scatterers. We considered a radar positioned above the cloud (e.g. aircraft or satellite) so that the cumulative attenuation is calculated from the top down to the surface. In logarithmic units and after integrating the attenuation over the range r, i.e. $dBZ = 10\log_{10}(Z)$ and $A = 10\log_{10}(e)\int 2k\mathrm{d}r$, this relationship becomes

$$dBZ(f) = dBZ_e(f) - A_h(f) - A_g(f). \tag{4}$$

The gaseous attenuation, A_g, is computed following Rosenkranz (1998) with the pressure, temperature, and humidity profiles from the VOCALS simulations as inputs to the algorithm. The equivalent reflectivity factor and the hydrometeor extinction are written in terms of the DSD as (Meneghini et al., 2003)

$$Z_e(f) = \frac{c^4}{\pi^5 f^4 |K_w(f)|^2} \int \sigma_b(f, D) N(D) \mathrm{d}D, \tag{5}$$

$$k_h(f) = \int \sigma_e(f, D) N(D) \mathrm{d}D, \tag{6}$$

where c is the speed of light. σ_b and σ_e are the backscattering and extinction cross-sections, respectively, computed using Mie electromagnetic theory (Bohren and Huffman, 1998). K_w is the dielectric factor of water, $K_w = (\varepsilon_w^2 - 1)/(\varepsilon_w^2 + 2)$. Using the empirical model described in Ray (1972), for liquid spheres at a temperature of 280 K, the complex permittivity is calculated to be $\varepsilon_{w,W} = 3.06 - 1.63i$ at W-band and $\varepsilon_{w,G} = 2.50 - 0.98i$ at G-band. The integrals in Eq. (5) and (6) are performed with an

https://doi.org/10.5194/egusphere-2025-4248
Preprint. Discussion started: 12 September 2025

upper/lower drop diameter limit of 50 μm as the distinction between the cloud/rain modes. Z_e and k_h are obtained for the cloud and rain modes separately, then added together in the regions where both modes coexist.

The resulting simulated radar reflectivities at W-band and G-band are presented in Fig. 3, which also shows the dual frequency reflectivity ratio (*DFR*) between both frequencies, simply defined as $DFR = dBZ_W - dBZ_G$. The maximum reflectivity values are around 10 dBZ at W-band and -5 dBZ at G-band, while the differential signal can reach values as large as 25 dB. It is worth noting that the computed two-way cumulative differential gaseous attenuation is approximately 8 dB at the surface, which indicates that even though the contribution from gaseous absorption to the observed *DFR* is important, the differential signal due to backscattering and extinction from drizzle drops can become larger than 15 dB. This is a strong differential signal that will help constrain drizzle properties to achieve more accurate retrievals.

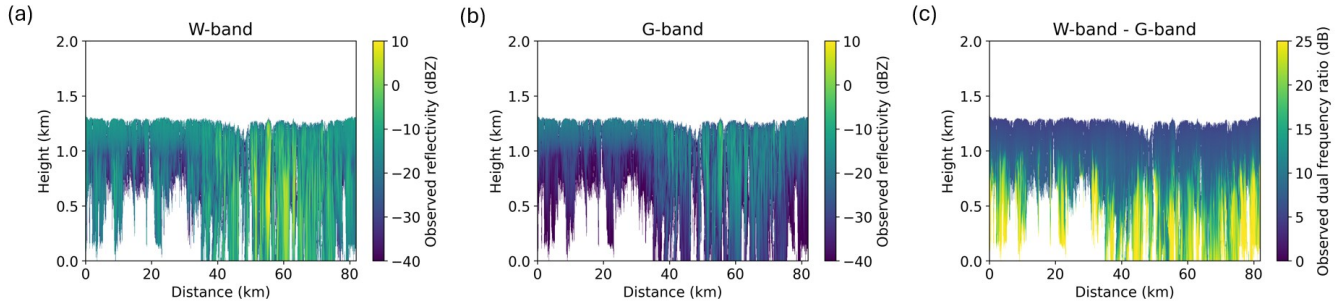

Figure 3: Simulated observed reflectivity at (a) W-band and (b) G-band, and (c) the dual-frequency reflectivity ratio between them.

2.3 Validation of simulated reflectivity

The Cloud and Precipitation Experiment at kennaook (CAPE-k; Mace et al., 2023) was a year-long field campaign located on the northwestern tip of Tasmania, Australia, that hosted multiple atmospheric instruments, including the Marine W-band ARM Cloud Radar (MWACR; Feng et al., 2024) and the CloudCube G-band radar (Socuellamos et al., 2024a). For the sole purpose of comparison and validation of the simulated radar observations, we show in Fig. 4 a one-hour fragment of real W-band and G-band observations that were taken during CAPE-k. We selected a low-level marine layer cloud producing drizzle, similar to the simulated scenario in Fig. 3, and calculated the gaseous absorption using the temperature, pressure, and humidity profiles obtained by an in-situ radiosonde launched two hours before the observation window. The gaseous attenuation was then subtracted from the observed reflectivities, inverted from top to bottom, and reapplied to depict observations from an imaginary radar above the scene. Even though the extinction by hydrometeors was not computed nor inverted, the similarities between Fig. 3 and Fig. 4 are recognizable, indicating that the simulated radar observations are representative of the dual-frequency response to real-world drizzling boundary layer clouds.

https://doi.org/10.5194/egusphere-2025-4248
Preprint. Discussion started: 12 September 2025

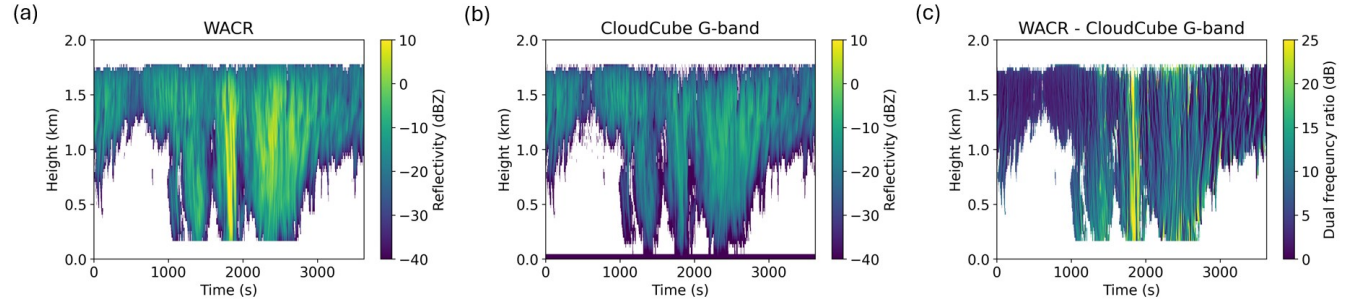

Figure 4: (a) W-band, (b) G-band and (c) *DFR* observations during the CAPE-k field campaign with inverted gaseous attenuation to simulate how they would be observed from above.

3. Optimal estimation framework

One of the main challenges of remote sensing instruments is to transform the observed signals into meaningful physical variables. A variety of retrieval algorithms has been developed over the years for that purpose (Stephens, 1994; Rodgers, 2000; Aster et al., 2018). They have mainly been focused on two different approaches: (1) statistically inferring the state variable, **x**, from the observation, **y**, through empirical relationships, or (2) connecting state and observation variables through a physical forward model. Optimal estimation is a physical retrieval methodology widely adopted in the atmospheric radar community to profile cloud and precipitation variables (Löhnert et al., 2004; Lebsock and L'Ecuyer, 2011; Mace et al., 2016; Maahn et al., 2020). Its strength stems from the fact that this approach not only allows the retrieval of hydrometeor properties but also the uncertainties associated with the retrieval. Optimal estimation is a probabilistic optimization involving covariance matrices describing measurement and prior uncertainties. How the matrices are constructed is critical to correctly represent the posterior uncertainties associated with the retrieval. The formulation of the covariance matrices is defined in Sect. 3.1, 3.2, and 3.3, however, before describing the details, we note here that it is not our intention to provide an unequivocal representation of the covariance matrices, as we acknowledge that these matrices can be constructed following several different perspectives (Rodgers, 2000; Maahn et al., 2020). The objective of this work is to compare two scenarios using the optimal estimation framework so that assumptions are common across both cases. Specifically, this study compares simulated dual-frequency W-band and G-band retrievals and W-band only retrievals. This comparison demonstrates that the synergies of simultaneous, dual-frequency W-band and G-band observations provide more accurate retrievals of drizzle properties than can be obtained from single-frequency approaches.

Our observation vectors, one for each vertical cloud and precipitation profile, comprise the W-band reflectivity, dBZ_W, the differential reflectivity, *DFR*, the path-integrated attenuation at W-band, PIA_W, and the differential path-integrated attenuation, *DPIA*. Each observation vector is then written as

$$\mathbf{y} = (dBZ_W(0), \ldots, dBZ_W(n), DFR(0), \ldots, DFR(n), PIA_W, DPIA)^{\mathrm{T}}, \quad (7)$$

https://doi.org/10.5194/egusphere-2025-4248
Preprint. Discussion started: 12 September 2025

with dimensions $2n + 2$ where n is the number of range gates in each cloud and precipitation profile. The state vector, on the other hand, includes the drizzle variables of interest, namely the mixing ratio, q_r, and the droplet concentration, N_r, and has dimensions $2n$

$$\mathbf{x} = (q_r(0), \dots, q_r(n), N_r(0), \dots, N_r(n))^{\mathrm{T}}. \quad (8)$$

The uncertainty matrix of the retrieved state vector, $\mathbf{S_x}$, is defined as

$$\mathbf{S_x} = (\mathbf{K^T S_e^{-1} K} + \mathbf{S_a^{-1}})^{-1}, \quad (9)$$

following the nomenclature in Rodgers (2000) and Maahn et al. (2020). $\mathbf{S_x}$ is a bidimensional matrix with dimensions $2n$ x $2n$. The Jacobian matrix, $\mathbf{K} = \partial\mathbf{y}/\partial\mathbf{x}$, is used to invert the forward model that maps state variables to observations, while the effective measurement covariance matrix, $\mathbf{S_e}$, and the a priori state covariance matrix, $\mathbf{S_a}$, describe the uncertainties related to the observation and a priori state assumption, respectively. A general approach to constructing these matrices is explained in Sect. 3.1, 3.2, and 3.3, while a particular example using a notional spaceborne dual-frequency radar is given in Sect. 5.

3.1 Effective observation covariance matrix

The effective observation covariance matrix, $\mathbf{S_e}$, is a square bidimensional matrix with dimensions $(2n + 2)$ x $(2n + 2)$ as per the length of the observation vector. The diagonal elements represent the i^{th} range-gate variance, $S_e(i,i) = \sigma_e^2(i)$, with the exception of the last two elements which correspond to the *PIA* uncertainties. The off-diagonal elements are the covariances between different range gates that, for simplicity, are assumed to be uncorrelated $S_e(i,j) = 0$.We acknowledge that in reality there may be significant correlation in the off-diagonal matrix elements that reflect the spatial correlation length scales of cloud and precipitation properties, however it can be challenging to accurately define these quantities (Maahn et al., 2020).

$\mathbf{S_e}$ can be more explicitly split into two additional matrices that contain the uncertainties related to the measurements themselves, $\mathbf{S_y}$, and those related to the forward model, $\mathbf{S_b}$. Starting with the instrument observation covariance matrix, $\mathbf{S_y}$, we consider three sources of uncertainty that arise from (1) the radar measurement random error, (2) the radar measurement systematic error, and (3) the uncertainty in the gaseous attenuation determination. The uncertainty in the reflectivity measurement due to random error can be calculated as (Doviak and Zrnić, 1993)

$$\sigma_{dBZ,r} = 10\log_{10}(e)\sqrt{\frac{1}{N_p}\left(\frac{N_p}{N_i} + \frac{2}{SNR} + \frac{1}{SNR^2}\right)}, \quad (10)$$

where N_p is the number of radar pulses averaged, N_i is the number of statistically independent pulses that can be calculated following Hogan et al. (2005), and *SNR* is the signal-to-noise ratio. Without defining any particular radar configuration at this time (we will provide a detailed example in Sect. 5), we assume $N_p = 100$, that all radar pulses are independent, $N_p/N_i = 1$, and that the *SNR* is large enough, $2/SNR + 1/SNR^2 \ll 1$, so that the random error can be simply approximated by a constant value, $\sigma_{dBZ,r} \approx \log_{10}(e)$ dB = 0.43 dB, across the cloud and precipitation profiles. The radar systematic or calibration error is taken to be $\sigma_{dBZ,s}$ = 1 dB based on CloudSat, ground-based, and airborne reflectivity analyses (Protat et al., 2009). Finally, we consider a 20% error in the derived profile of the water vapor attenuation, $\delta_{Ag} = 0.2A_g$, where we have conservatively inflated the typical

https://doi.org/10.5194/egusphere-2025-4248
Preprint. Discussion started: 12 September 2025

values of 4% - 8% found in modern infrared sounding products in the lower troposphere (Trent et al., 2019). The uncertainty in the dual-frequency reflectivity ratio is $\sigma_{DFR} = (\sigma_{dBZ,W}^2 + \sigma_{dBZ,G}^2)^{1/2}$ while $\sigma_{PIA,W}$ and $\sigma_{DPIA} = (\sigma_{PIA,W}^2 + \sigma_{PIA,G}^2)^{1/2}$ use the surface return and integral quantities to compute the uncertainties.

The forward model uses the equations and parameters described in Sect. 2.2 to link observation and state vectors. There are three independent physical variables in the assumed gamma DSD (q_c, N_c, and μ) whose uncertainty needs to be included in the forward covariance matrix, $\mathbf{S_b}$. In practice, q_c and N_c can vary within several orders of magnitude and μ can also present a great disparity of values. These forward model uncertainties are perhaps the most challenging to quantify and many retrieval algorithms prefer to ignore this term to construct the effective observation covariance matrix (Maahn et al., 2020). The type of clouds that we are targeting in this work have been studied in recent years by spaceborne instruments and through airborne campaigns (Rauber et al., 2007; Mace et al., 2016; Mroz et al., 2023). These data sets can be used to constrain and provide a reasonable range of values for the forward model parameters through the analysis of similar events. For example, cloud optical properties derived from reflected sunlight can constrain a vertical profile of q_c and N_c in thin stratiform clouds (Grosvenor et al., 2018). We have thus assumed that it should be possible to estimate q_c, N_c, and μ, within a 50% uncertainty, and have incorporated these errors into $\mathbf{S_b}$.

With all the variances already defined, the first $2n$ diagonal elements of the effective observation covariance matrix, $S_{e,\mathbf{y}}(i,i) = S_{y,\mathbf{y}}(i,i) + S_{b,\mathbf{y}}(i,i)$, take the form of

$$S_{y,\mathbf{y}}(i,i) = \sigma_{\mathbf{y},r}^2(i) + \sigma_{\mathbf{y},s}^2(i) + \left(\frac{\partial \mathbf{y}(i)}{\partial A_g}\delta A_g\right)^2, \tag{11}$$

$$S_{b,\mathbf{y}}(i,i) = \left(\frac{\partial \mathbf{y}(i)}{\partial q_c}\delta q_c\right)^2 + \left(\frac{\partial \mathbf{y}(i)}{\partial N_c}\delta N_c\right)^2 + \left(\frac{\partial \mathbf{y}(i)}{\partial \mu}\delta \mu\right)^2. \tag{12}$$

where $\mathbf{y}$ represents the different variables in the observation vector. Then, each matrix becomes

$$\mathbf{S_e} = \begin{pmatrix} S_{e,dBZ_W}(0,0) & \cdots & 0 & 0 & \cdots & 0 & 0 & 0 \\ \vdots & \ddots & 0 & 0 & \cdots & 0 & 0 & 0 \\ 0 & 0 & S_{e,dBZ_W}(n,n) & 0 & \cdots & 0 & 0 & 0 \\ 0 & 0 & 0 & S_{e,DFR}(0,0) & \cdots & 0 & 0 & 0 \\ \vdots & \vdots & \vdots & \vdots & \ddots & 0 & 0 & 0 \\ 0 & 0 & 0 & 0 & 0 & S_{e,DFR}(n,n) & 0 & 0 \\ 0 & 0 & 0 & 0 & 0 & 0 & S_{e,PIA_W} & 0 \\ 0 & 0 & 0 & 0 & 0 & 0 & 0 & S_{e,DPIA} \end{pmatrix}. \tag{13}$$

As an example, for the first vertical cloud and precipitation profile, the matrix results are shown in Fig. 5. In this case, the vertical profile has 231 range gates, and the matrix dimensions are 464 x 464. The first 231 diagonal elements are the variances corresponding to the dBZ_W measurement, which increase from the surface to the cloud top due mainly to the error sources related to q_c and N_c that are only present in the cloud mode. The second 231 diagonal elements represent the variances related to the *DFR* observation. Here, the main contribution to the error is the differential gaseous attenuation, which increases

https://doi.org/10.5194/egusphere-2025-4248
Preprint. Discussion started: 12 September 2025

240 towards the surface. Finally, the last two diagonal elements contain the variance of the path integrated absorption at W-band and the differential path integrated absorption.

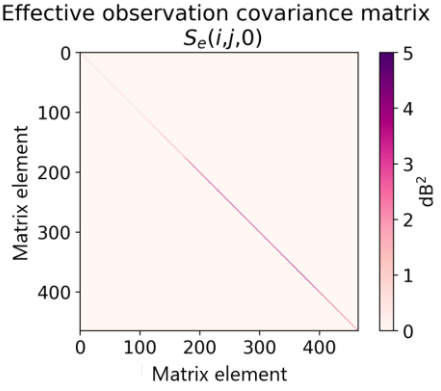

Figure 5: Effective observation covariance matrix of the first cloud and precipitation vertical profile.

245

3.2 Jacobian matrix

The Jacobian matrix, **K**, has dimensions $(2n + 2)$ x $2n$, and is formed by the partial derivatives that relate state and observation vectors across the different range gates of a vertical cloud and precipitation profile. Overall, the matrix takes the following form

250
$$\mathbf{K} = \begin{pmatrix} \frac{\partial dBZ_W(0)}{\partial q_r(0)} & \cdots & \frac{\partial dBZ_W(0)}{\partial q_r(n)} & \frac{\partial dBZ_W(0)}{\partial N_r(0)} & \cdots & \frac{\partial dBZ_W(0)}{\partial N_r(n)} \\ \vdots & \ddots & \vdots & \vdots & \ddots & \vdots \\ 0 & \cdots & \frac{\partial dBZ_W(n)}{\partial q_r(n)} & 0 & \cdots & \frac{\partial dBZ_W(n)}{\partial N_r(n)} \\ \frac{\partial DFR(0)}{\partial q_r(0)} & \cdots & \frac{\partial DFR(0)}{\partial q_r(n)} & \frac{\partial DFR(0)}{\partial N_r(0)} & \cdots & \frac{\partial DFR(0)}{\partial N_r(n)} \\ \vdots & \ddots & \vdots & \vdots & \ddots & \vdots \\ 0 & \cdots & \frac{\partial DFR(n)}{\partial q_r(n)} & 0 & \cdots & \frac{\partial DFR(n)}{\partial N_r(n)} \\ \frac{\partial PIA_W}{\partial q_r(0)} & \cdots & \frac{\partial PIA_W}{\partial q_r(n)} & \frac{\partial PIA_W}{\partial N_r(0)} & \cdots & \frac{\partial PIA_W}{\partial N_r(n)} \\ \frac{\partial DPIA}{\partial q_r(0)} & \cdots & \frac{\partial DPIA}{\partial q_r(n)} & \frac{\partial DPIA}{\partial N_r(0)} & \cdots & \frac{\partial DPIA}{\partial N_r(n)} \end{pmatrix}, \quad (14)$$

with $(\partial dBZ_W(j)/\partial q_r(i))_{j>i} = 0$, $(\partial dBZ_W(j)/\partial N_r(i))_{j>i} = 0$, $(\partial DFR(j)/\partial q_r(i))_{j>i} = 0$, and $(\partial DFR(j)/\partial N_r(i))_{j>i} = 0$, as changes in the state vector below the observed range gate will not affect the radar measurements.

The Jacobian matrix of the first profile for the case under study is shown in Fig. 6 (refer to Eq. (14) to identify the 255 element ordering). By looking first at the left half of the matrix, that contains the partial derivatives of the observation vector

https://doi.org/10.5194/egusphere-2025-4248
Preprint. Discussion started: 12 September 2025

with respect to the rain mixing ratio, the two sub-diagonals are positive, meaning that a variation in q_r has a direct effect on the observation vector. For example, if q_r increases, we expect a stronger backscattering response from the hydrometeors and, since we can assume Mie regime for drizzle sizes at G-band, the differential signal will also increase. On the other hand, the off-diagonal elements can be either positive or negative depending on whether we are using single-frequency or dual-frequency observations. The off-diagonal elements include the changes due to the propagation of the hydrometeor extinction and, while radar signal echoes become more attenuated if q_r increases and therefore the variation becomes negative, the hydrometeor absorption is stronger at G-band, which leads to differential absorption variations that are positive. The right half of the matrix shows the changes in the observation vector relative to the rain drop number concentration. In this case, the sub-diagonals are mostly negative. This can be explained bearing in mind that, for instance, if N_r increases while keeping q_r fixed, that necessarily means that drops become smaller and both *dBZ* and *DFR* decrease. The off-diagonal elements have a variable behaviour, precisely due to the change in the drop sizes that can lead to a diverse response in the absorption by hydrometeors.

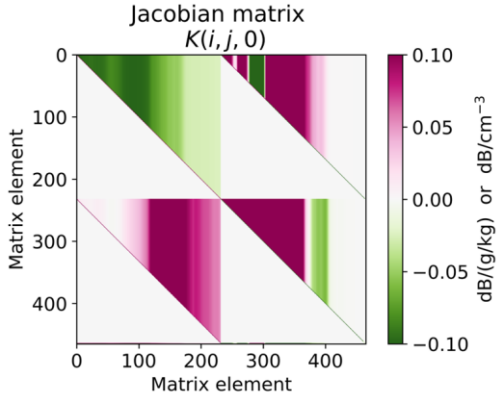

Figure 6: Jacobian matrix of the first cloud and precipitation profile.

3.3 A priori state covariance matrix

The a priori state covariance matrix, $\mathbf{S_a}$, has dimensions $2n$ x $2n$ and contains the uncertainties related to the prior knowledge of the vector state for a single vertical atmospheric profile. The prior assumptions serve to constrain the retrieval, and therefore need to be carefully quantified to avoid potentially biased results. In a similar approach as to the assumed uncertainties in the forward model parameters in $\mathbf{S_b}$ (see Sect. 3.1), we have considered that an educated guess of the a priori state can be derived from existing observations of similar events and model simulations. In this instance, instead of assigning a fixed relative uncertainty to all data points, we followed a variable approach to better represent the uncertainties over several orders of magnitude. Using the rain mixing ratio and drop concentration from the VOCALS simulations (see Fig. 2(d) and Fig. 2(e)), the diagonal of the a priori covariance matrix is constructed with the square root of the q_r and N_r values as uncertainties. This allows us to scale the uncertainties based on the magnitude of the prior values, giving lower uncertainties to heavier drizzle regions and larger uncertainties to very weak drizzle. Minimum and maximum relative a priori uncertainty values are

https://doi.org/10.5194/egusphere-2025-4248
Preprint. Discussion started: 12 September 2025

in the order of 100% and 10000%, respectively. The first n diagonal elements contain the variances for the a priori q_r, while the last n diagonal elements are the variances for the a priori N_r. The off-diagonal elements are set to zero for simplicity. Then, the a priori covariance matrix results in

$$\mathbf{S_a} = \begin{pmatrix} S_{a,q_r}(0,0) & \cdots & 0 & 0 & \cdots & 0 \\ \vdots & \ddots & \vdots & \vdots & \ddots & \vdots \\ 0 & \cdots & S_{a,q_r}(n,n) & 0 & \cdots & 0 \\ 0 & \cdots & 0 & S_{a,N_r}(0,0) & \cdots & 0 \\ \vdots & \ddots & \vdots & \vdots & \ddots & \vdots \\ 0 & \cdots & 0 & 0 & \cdots & S_{a,N_r}(n,n) \end{pmatrix}. \quad (15)$$

To give an example, the a priori state covariance matrix of the first cloud and precipitation profile is shown in Fig. 7.

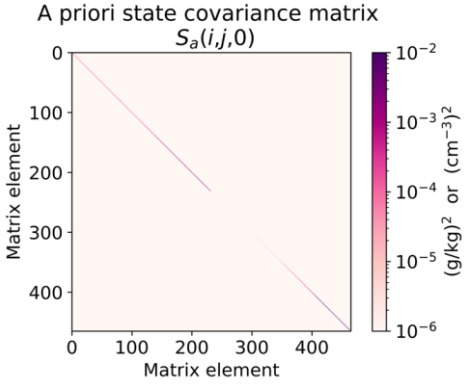

Figure 7: A priori state matrix of the first cloud and precipitation profile.

4. Retrieval uncertainty

Once all the matrices are constructed as shown in Sect. 3.1, 3.2, and 3.3, we only need to incorporate them into Eq. (9) to compute the posterior uncertainty covariance matrix of the retrieved atmospheric state. As we are interested in the potential improvement that the simultaneous W-band and G-band observations can bring to the drizzle retrieval, we have executed the algorithm first using the simulated dual-frequency observations and second using only W-band observations. The results and comparison of both approaches are discussed in Sect. 4.1, 4.2 and 4.3.

4.1 W-band and G-band retrieval

Figure 8 shows the posterior state covariance matrices for three different cloud and precipitation profiles, namely the 0^{th}, 10^{th} and 100^{th} profiles. Given the range of values that span several orders of magnitude, the results are plotted in logarithmic units multiplied by the sign of the value. The matrices are symmetric with positive diagonal elements, as expected by the definition of a covariance matrix. Their first n diagonal elements contain the variance of the retrieved rain mixing ratio at the

https://doi.org/10.5194/egusphere-2025-4248
Preprint. Discussion started: 12 September 2025

i^{th} range gate, $\sigma_{q_r}^2(i)$, while the last n diagonal elements are the variance of the rain drop concentration, $\sigma_{N_r}^2(i)$. The off-diagonal elements are the covariances, $\rho(i,j)\sigma_{q_r}(i)\sigma_{N_r}(j)$, where ρ is the correlation between the posterior uncertainty in the state vector variables. Most of the covariances in Fig. 8 are positive (red values), meaning that both errors vary together and are positively correlated. In some cases, the covariances may be negative (blue values), and errors vary in opposite directions and are anticorrelated. This transition between positive and negative covariances could be due to regions in the cloud and precipitation profile where drops are either too small or too large that the *DFR* signal does not provide substantial new information and the retrieval becomes under constrained. Uncertainties tend to be smaller towards the first indices of the cloud and precipitation profile (close to the surface) where drizzle is predominant and attenuation is stronger.

If we extract the main diagonal of every computed $\mathbf{S_x}$, we can get the uncertainty in the retrieved q_r and N_r for every cloud and precipitation profile. From q_r, N_r, and the mass-diameter relationship for spherical liquid drops, we can also derive the mass-weighted diameter of the drizzle drops, D_r, as

$$D_r = \left(\frac{\rho_a q_r}{a_m N_r}\right)^{\frac{1}{b_m}}, \tag{16}$$

and also calculate its uncertainty, σ_{Dr}, following standard propagation of errors including q_r and N_r variance and covariance terms. The uncertainties for q_r, N_r, and D_r, are shown in the top three panels of Fig. 9, while their relative error with respect to the true values from the VOCALS simulations are presented in the bottom three panels of Fig. 9. If we compare these plots with panel (c) in Fig. 3, we can see how the lower uncertainty near the surface corresponds to regions where the observed *DFR* values are non-zero. This is a clear indication of the benefits of adding a second frequency radar channel and including *DFR* and *DPIA* in the optimal estimation algorithm. In particular, the combination of W-band and G-band frequencies, where there exists a measurable and positive monotonic differential backscattered signal for drizzle drop diameters in the range 100 μm – 300 μm, provides the additional constraints needed to improve the retrieval accuracy in lightly precipitating events.

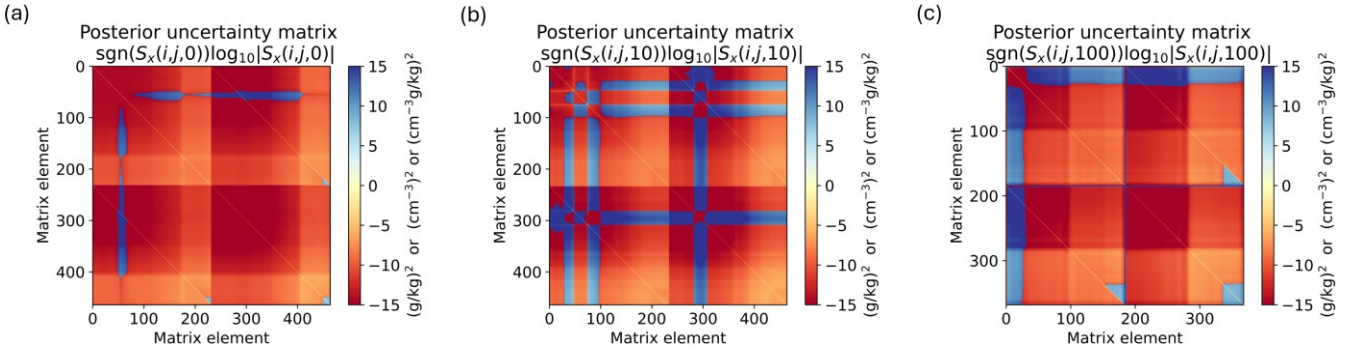

Figure 8: Posterior uncertainty matrices of the (a) 0th, (b) 10th and (c) 100th profiles.

https://doi.org/10.5194/egusphere-2025-4248
Preprint. Discussion started: 12 September 2025

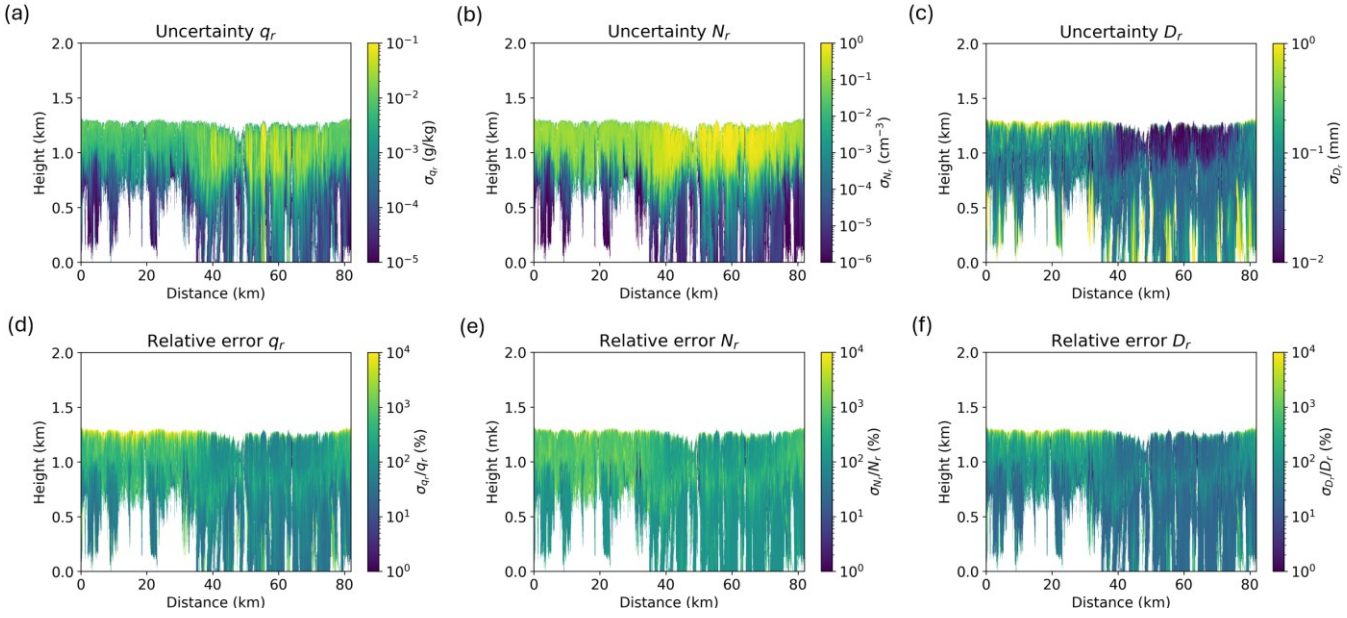

Figure 9: Uncertainty (top) and relative error (bottom) in the retrieval of the drizzle mixing ratio (left), drop number concentration (center) and mass-weighted mean drop diameter (right).

330

4.2 W-band only retrieval

To compute the uncertainties using only W-band measurements, the matrices are reconstructed with an observation vector that takes the form of $\mathbf{y_W} = (dBZ_W(0), \ldots, dBZ_W(n), PIA_W)^T$, and matrix dimensions that were $2n$ or $2n+2$ now become n or $n+1$, respectively. The uncertainties and relative errors for q_r, N_r, and D_r obtained using only W-band observations are
335 shown in Fig. 10. By comparing Fig. 10 to Fig. 9, we can see that there is a substantial increase in the uncertainty of the retrieved parameters precisely where the *DFR* signal is stronger (see panel (c) in Fig. 3). Without the additional constraints provided by the addition of the G-band frequency channel, the algorithm considerably worsens at determining q_r, N_r, and D_r in the drizzle region.

https://doi.org/10.5194/egusphere-2025-4248
Preprint. Discussion started: 12 September 2025

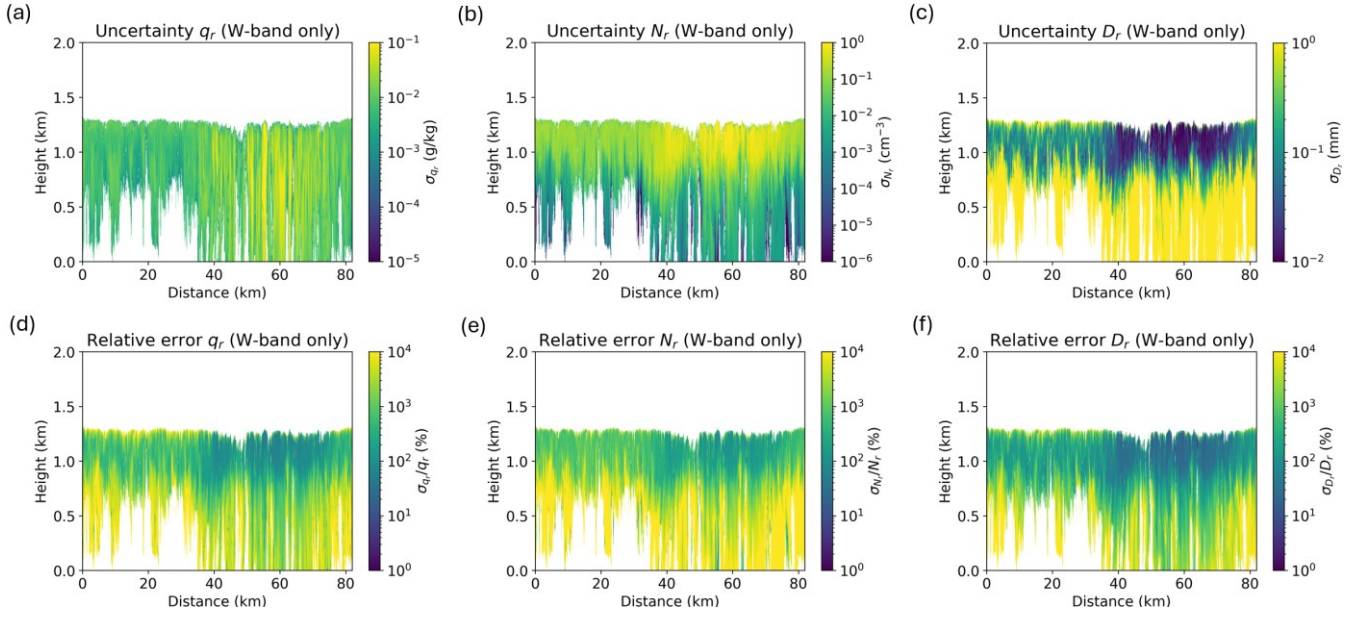

Figure 10: Uncertainty (top) and relative error (bottom) in the retrieval of the drizzle mixing ratio (left), drop number concentration (center) and mass-weighted mean drop diameter (right) using only W-band measurements.

4.3 Comparison between W-band and G-band and W-band only retrievals

To provide a better understanding of the improvement in the retrieval by performing W-band and G-band simultaneous observations instead of only W-band measurements, we have examined the distribution of the q_r, N_r, and D_r relative errors shown in the bottom plots of Fig. 9 and 10 through the probability density function (PDF) for each of them. The normalized PDFs are shown in Fig. 11 while the most relevant parameters, i.e. mode, median, and mean, are provided in Table 1. Overall, in Fig. 11, it is obvious that the W-band only relative errors are substantially larger than those obtained with the dual-frequency radar system. Specifically, the median, perhaps the best representative quantity given the large dispersion of errors, is reduced by more than one order of magnitude if differential measurements are considered.

Another parameter used to quantify the uncertainty of the state variables is the information content of the retrieval. Defined as (Rodgers, 2000)

$$\mathbf{H} = \frac{1}{2}\log_2\left(\frac{\mathbf{S_a}}{\mathbf{S_x}}\right), \tag{17}$$

the information content matrix, **H,** describes how important observation variables are to improve the knowledge of the state variables. For example, a low information value (close to zero) means that the posterior state heavily depends on the a priori assumptions and that the observations barely provide any new knowledge to constrain the retrieval. If the information content is large, then the retrieval is driven by the measurements, potentially avoiding biases if the knowledge of the prior state is not reliable. In Fig. 12, we show how the information content of the retrieval, represented as the median of **H** for all the cloud and

https://doi.org/10.5194/egusphere-2025-4248
Preprint. Discussion started: 12 September 2025

precipitation profiles, depends on the a priori state uncertainty. As our confidence in the knowledge of the a priori state gets worse, the dual-frequency observations become increasingly important. In particular, for the a priori covariance matrix described in Sect. 3.3 (note that we defined a variable relative uncertainty and that the stars in Fig. 12 point at the median of those different relative uncertainties), the W-band and G-band pair provides more than ten times additional information than the W-band only retrieval.

These results indicate again the importance of complementary W-band and G-band observations to better constrain the optimal estimation framework and achieve a notable reduction in the retrieval uncertainty of drizzle parameters.

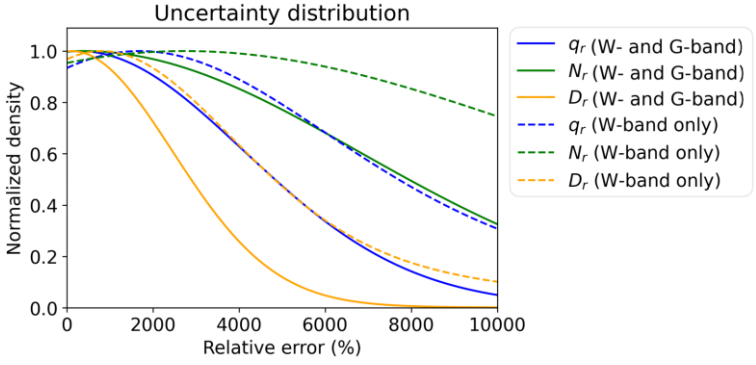

Figure 11: Normalized density function of the retrieved relative errors using W-band and G-band observations (solid lines) and only W-band (dashed lines).

Table 1: Statistical comparison between W-band and G-band and W-band only retrievals.

	W-band and G-band	W-band only
	σ_{qr}/q_r (%)	
Mode	383	1717
Median	108	1312
Mean	926	3797
	σ_{Nr}/N_r (%)	
Mode	404	2727
Median	190	2099
Mean	994	10003
	σ_{Dr}/D_r (%)	
Mode	101	808
Median	38	500
Mean	404	3026

https://doi.org/10.5194/egusphere-2025-4248
Preprint. Discussion started: 12 September 2025

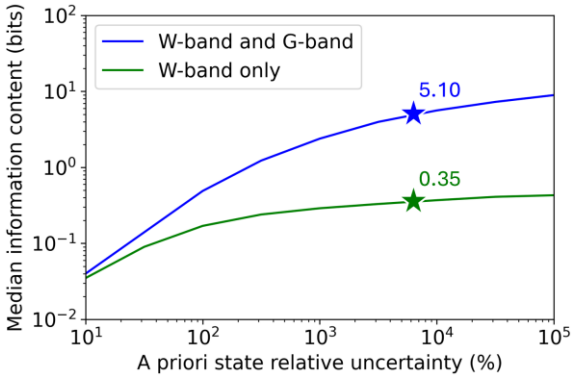

Figure 12: Median information content for the W-band and G-band retrieval and W-band only retrieval assuming different a priori state relative uncertainties. The median information content for the retrieval corresponding to the uncertainties in Table 1 is highlighted with stars.

5. Application to a notional spaceborne W-band and G-band radar

A relevant scenario where the methodology could be applied is a notional dual-frequency W-band and G-band spaceborne radar designed to improve estimates of global precipitation. The optimal estimation framework can be applied to realistic spaceborne observations as long as the limitations in sensitivity and horizontal and vertical resolution of the instrument are considered. To adapt the simulated observations shown in Fig. 3, we need first to define the performance and parameters of our spaceborne dual-frequency radar concept. We envision an instrument deployed in low-Earth orbit (LEO) at an altitude of 450 km whose performance is tailored to detect and profile low-level shallow warm clouds and drizzle. In that case, we are interested in measuring cloud and precipitation profiles with fine resolution where the characteristic low dBZ values of this type of scenes are detectable. The radars operate using pulse compression to facilitate both objectives, and target vertical resolution < 100 m and sensitivity < -15 dBZ. Based on these requirements and the availability of state-of-the-start technology, the radar parameters are defined in Table 2. Peak transmit power of 100 W at W-band is readily obtainable from recently developed solid-state sources (Soric et al., 2022) while 50 W at G-band could be achieved after scaling lower-frequency high-power vacuum sources (Field et al., 2018). Receiver noise figures of 4 dB at W-band and 5.5 dB at G-band can be achieved with available low-noise amplifiers (LNAs) (Kangaslahti et al., 2012; Cuadrado-Calle et al., 2024). The W-band and G-band channels operate independently but share a common 2-m Cassegrain reflector antenna with one of the feed horns positioned slightly offset at the expense of a small gain penalty (< 1 dB) and along-track mismatch (< 10 km). With a spacecraft orbital speed of 7.7 km/s, both radar channels probe the same cloud's along-track volume within approximately one second, before any appreciable atmospheric changes occur. Assuming no losses from the transmitter source to the feed or from the feed to the LNA and antenna efficiency factors of 60% and 50% at W-band and G-band, respectively, antenna directivities are calculated to be 62 dBi at W-band (including a 1.5 dB feed offset loss) and 71 dBi at G-band. With a 2-m antenna size, the instantaneous radar along-track footprint is 875 m at W-band and 345 m at G-band. The pulse width is chosen to be 150 μs at W-band and

https://doi.org/10.5194/egusphere-2025-4248
Preprint. Discussion started: 12 September 2025

75 μs at G-band, both radars transmitting at 10% duty cycle. 50 pulses at W-band and 100 pulses at G-band are incoherently averaged for a total integration time of 75 ms. After accounting for the integration time, the along-track resolution becomes approximately 1460 m at W-band and 920 m at G-band. While biases related to non-uniform beam filling and beam mismatch between both radar channels can be significant in highly turbulent or convective scenes, the relatively small footprints at W-band and G-band are viable for targeting stratocumulus which tend to be more homogeneous at the scale of a few kilometers. Finally, the chirp bandwidth is chosen to be 6 MHz at both channels, and the instrument range resolution is approximated to 50 m bearing in mind waveform and filter parametrizations (Beauchamp et al., 2016). Considering all these specifications, the minimum measurable reflectivity is estimated to be -21 dBZ at W-band and -30 dBZ at G-band.

To apply the spaceborne configuration to the simulated observations from Fig. 3, we averaged a number of range gates in the original data to achieve the required range resolution. The horizontal cells were also averaged, but with a Gaussian weight function to account for the radar beam pattern. Any resulting reflectivity points with values below -21 dBZ at W-band and -30 dBZ at G-band were masked out. Finally, following simulations of the radar point target response after assuming a surface cross section (σ_0) of 10 dB, we approximate the first 150 m to be dominated by surface clutter and, therefore, these are also removed. With all these details taken into consideration, the resulting spaceborne simulated observations of the proposed dual-frequency radar concept are shown in Fig. 13. Comparing with Fig. 3, a large fraction of the cloud and precipitation in this type of atmospheric events can still be detected with this notional spaceborne instrument, including easily discernible *DFR* signals that can reach 25 dB due to the combination of hydrometeor and gaseous differential effects.

The state and observation vectors, as well as the various matrices of the optimal estimation framework, are constructed and populated in an identical form as that described in Sect. 3. The only differences come from the shorter length that the cloud and precipitation profiles now have, and the reduced number of profiles. In Fig. 14, we present the relative errors in uncertainties for q_r, N_r, and D_r, after executing the algorithm for the notional spaceborne case, including W-band and G-band, and W-band only results. Errors in the dual-frequency retrieval are seen to increase compared to those obtained in Fig. 9 due to the non-uniform beam filling and the beam mismatch of a realistic spaceborne scenario. Nevertheless, uncertainties are still significantly lower relative to the W-band only results, showing that a substantial improvement in the retrieval of drizzle properties can be attained compared to existing spaceborne W-band cloud radars (e.g. CloudSat and EarthCARE).

https://doi.org/10.5194/egusphere-2025-4248
Preprint. Discussion started: 12 September 2025

Table 2: Radar parameters of the notional spaceborne W-band and G-band system.

	W-band	G-band
Peak transmit power (W)	100	50
Pulse width (μs)	150	75
Pulse repetition interval (μs)	1500	750
Chirp bandwidth (MHz)	6	6
Receiver noise figure (dB)	4	5.5
Antenna directivity (dBi)	62	71
Range resolution (m)	50	50
Number of pulses averaged	50	100
Integration time (ms)	75	75
Along-track resolution (m)	1460	920
Minimum reflectivity (dBZ)	-21	-30

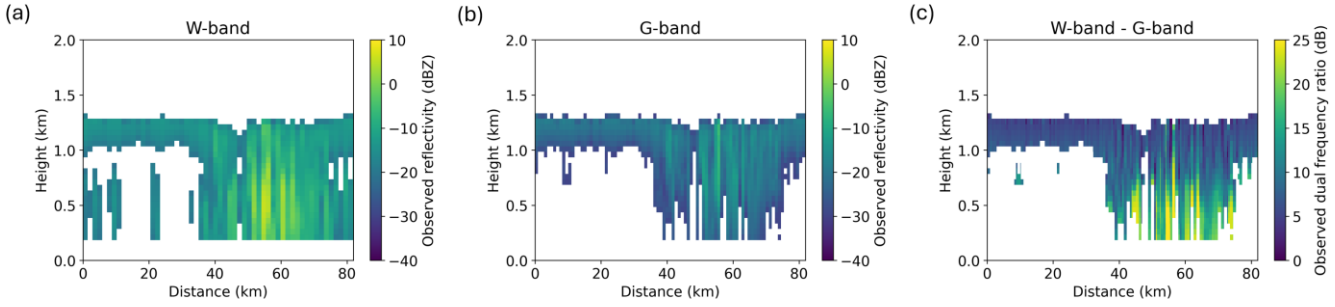

Figure 13: Simulated spaceborne observations for a dual-frequency radar concept based on the parameters from Table 2. (a) W-band observed reflectivity, (b) G-band observed reflectivity, and (c) dual-frequency reflectivity ratio.

https://doi.org/10.5194/egusphere-2025-4248
Preprint. Discussion started: 12 September 2025

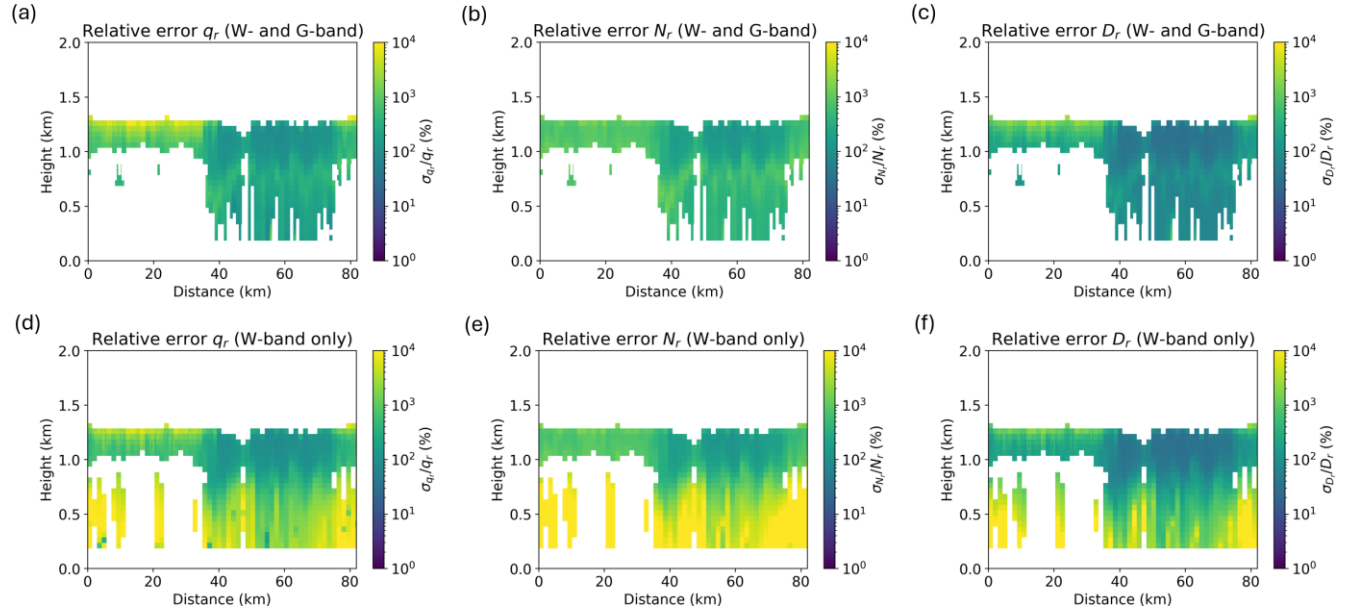

Figure 14: Relative error in the retrieval of the rain mixing ratio, drop concentration, and mass-weighted mean diameter for the notional spaceborne W-band and G-band (top) and W-band only (bottom) radars.

6. Summary and conclusion

Better quantification of precipitating water mass and sizing in shallow liquid clouds are critical to better understand the coupled hydrological and energy cycles and improve the fidelity of model simulations and predictions. Current instruments are challenged in identifying and measuring light precipitation in shallow clouds that are ubiquitous in the planetary boundary layer, particularly airborne and spaceborne radar measurements that have to account for platform motion on Doppler moments. Dual-frequency W-band and G-band radar measurements of the differential backscattering and attenuation by hydrometeors show promise in providing drop sizing and more accurate estimates of the mass of embryonic droplets in the localized sections where precipitation is initiated.

Using simulated nadir-looking radar observations of precipitating boundary layer clouds, we extended a conventional physical optimal estimation method to incorporate differential W-band and G-band measurements, namely the dual-frequency reflectivity ratio and the differential path-integrated attenuation. We evaluated the capabilities of these dual-frequency observations to constrain precipitation microphysics in drizzling stratocumulus. After constructing the covariance matrices and computing the retrieval algorithm, we found that the dual-frequency W-band and G-band radar system can provide an improvement of more than one order of magnitude in the retrieval accuracy of the drizzle mixing ratio, drop concentration, and mean diameter compared to a W-band only radar. Finally, we applied the algorithm to adapted observations obtained by a notional spaceborne radar, showing that current state-of-the-art technologies achieve sufficient sensitivity to provide significant constraint to estimate drizzle properties from LEO satellites. Overall, the errors from a spaceborne platform increase

https://doi.org/10.5194/egusphere-2025-4248
Preprint. Discussion started: 12 September 2025

relative to airborne due to non-uniform beamfilling and beam mismatch. However, the relative improvement of the W-band and G-band retrieval compared to W-band only is robust even from spaceborne observations.

It is now possible to achieve important advances in remote radar measurements of drizzle and light rain using multifrequency observations through the addition of a G-band radar channel. The first ground-based observations from G-band radars are recently available and airborne observations by NASA and ESA are anticipated in the near future. The methodology developed in this work can become a useful tool to be applied in multifrequency radar airborne deployments, and the quantitative findings can encourage further studies of the W-band and G-band radar pair as a potential spaceborne instrument to complement mission concepts.

Data availability

The following data sets can be acquired online following the references:

- VOCALS: Kurowski (2025).
- MWACR: Bharadwaj et al. (2024).
- CloudCube G-band: Socuellamos et al. (2025).
- Radiosonde: Jenssen et al. (2024).

Author contributions

MJK computed the VOCALS simulations and provided guidance on their utilization. DJP advised on the DSD implementation. RRM and RMB gave direction on the notional spaceborne radar parameters. JMS and MDL developed the optimal estimation retrieval algorithm. JMS composed the manuscript with contributions from the rest of the authors.

Competing interests

The authors declare that they have no conflict of interest.

Acknowledgements

This research was performed at the Jet Propulsion Laboratory, California Institute of Technology, under a contract with the National Aeronautics and Space Administration (80NM0018D0004).

MWACR and radiosonde data were obtained from the atmospheric radiation measurement (ARM) user facility, a U.S. department of energy (DOE) office of science user facility managed by the biological and environmental research program.

https://doi.org/10.5194/egusphere-2025-4248
Preprint. Discussion started: 12 September 2025

References

Abel, S. J. and Boutle, I. A.: An improved representation of the raindrop size distribution for single-moment microphysics schemes, Quarterly Journal of the Royal Meteorological Society, 138, 2151–2162, https://doi.org/10.1002/qj.1949, 2012.

Aster, R. C., Borchers, B., and Thurber, C. H.: Parameter Estimation and Inverse Problems. Elsevier, 406 pp., 2018.

Battaglia, A., Westbrook, C. D., Kneifel, S., Kollias, P., Humpage, N., Löhnert, U., Tyynelä, J., and Petty, G. W.: G band atmospheric radars: new frontiers in cloud physics, Atmospheric Measurement Techniques, 7, 1527–1546, https://doi.org/10.5194/amt-7-1527-2014, 2014.

Beauchamp, R. M., Tanelli, S., Peral, E., and Chandrasekar, V.: Pulse compression waveform and filter optimization for spaceborne cloud and precipitation radar, IEEE Transactions on Geoscience and Remote Sensing, 55, 915–931, https://doi.org/10.1109/tgrs.2016.2616898, 2016.

Berner, A. H., Bretherton, C. S., and Wood, R.: Large-eddy simulation of mesoscale dynamics and entrainment around a pocket of open cells observed in VOCALS-REx RF06, Atmospheric Chemistry and Physics, 11, 10525–10540, https://doi.org/10.5194/acp-11-10525-2011, 2011.

Bharadwaj, N., Hardin, J., Isom, B., and Matthews, A.: Marine W-Band Arm Cloud Radar (MWACRCFR), https://doi.org/10.5439/1512077, 2024.

Beard, K. V. and Ochs, H. T.: Warm-rain initiation: An overview of microphysical mechanisms. Journal of Applied Meteorology, 32(4), 608–625. https://doi.org/10.1175/1520-0450(1993)032<0608:WRIAOO>2.0.CO;2, 1993.

Bohren, C. F. and Huffman, D. R.: Absorption and scattering of light by small particles, https://doi.org/10.1002/9783527618156, 1998.

Courtier, B. M., Battaglia, A., Huggard, P. G., Westbrook, C., Mroz, K., Dhillon, R. S., Walden, C. J., Howells, G., Wang, H., Ellison, B. N., Reeves, R., Robertson, D. A., and Wylde, R. J.: First observations of G-Band radar Doppler spectra, Geophysical Research Letters, 49, https://doi.org/10.1029/2021gl096475, 2022.

Cuadrado-Calle, D., Kantanen, M., Valenta, V., and Ayllón, N.: A GAN-on-Si MMIC LNA for spaceborne cloud profiling radars and W-Band telecom links, IEEE Microwave and Wireless Technology Letters, 1–0, https://doi.org/10.1109/lmwt.2024.3469276, 2024.

Doviak, R. and Zrnić, D.: Doppler Radar and Weather Observations, second edn., Dover Publications, Inc., Mineola, NY, 1993.

Feng, Y.-C., Lindenmaier, I., Theisen, A., Wang, D., Collis, S., Tian, J., Silber, I., Gupta, S., Zhang, D., Mather, J., Comstock, J., Jackson, R., O'Brien, J., and Raut, B.: ARM FY2025 Radar Plan, U.S. Department of Energy, Atmospheric Radiation Measurement user facility, Richland, Washington, 2024.

Field, M., Kimura, T., Atkinson, J., Gamzina, D., Luhmann, N. C., Stockwell, B., Grant, T. J., Griffith, Z., Borwick, R., Hillman, C., Brar, B., Reed, T., Rodwell, M., Shin, Y.-M., Barnett, L. R., Baig, A., Popovic, B., Domier, C., Barchfield, R.,

https://doi.org/10.5194/egusphere-2025-4248
Preprint. Discussion started: 12 September 2025

Zhao, J., Higgins, J. A., and Goren, Y.: Development of a 100-W 200-GHz high bandwidth MM-Wave amplifier, IEEE Transactions on Electron Devices, 65, 2122–2128, https://doi.org/10.1109/ted.2018.2790411, 2018.

Grosvenor, D. P., Sourdeval, O., Zuidema, P., Ackerman, A., Alexandrov, M. D., Bennartz, R., Boers, R., Cairns, B., Chiu, J. C., Christensen, M., Deneke, H., Diamond, M., Feingold, G., Fridlind, A., Hünerbein, A., Knist, C., Kollias, P., Marshak, A., McCoy, D., Merk, D., Painemal, D., Rausch, J., Rosenfeld, D., Russchenberg, H., Seifert, P., Sinclair, K., Stier, P., Van Diedenhoven, B., Wendisch, M., Werner, F., Wood, R., Zhang, Z., and Quaas, J.: Remote Sensing of droplet number concentration in warm clouds: A review of the current state of knowledge and perspectives, Reviews of Geophysics, 56, 409–453, https://doi.org/10.1029/2017rg000593, 2018.

Hogan, R. J., Gaussiat, N. and Illingworth, A. J.: Stratocumulus liquid water content from dual-wavelength radar, J. Atmos. O. Tech., 22(8), 1207-1218. https://doi.org/10.1175/JTECH1768.1, 2005.

Iacono, M. J., Delamere, J. S., Mlawer, E. J., Shephard, M. W., Clough, S. A., and Collins, W. D.: Radiative forcing by long-lived greenhouse gases: Calculations with the AER radiative transfer models, Journal of Geophysical Research Atmospheres, 113, https://doi.org/10.1029/2008jd009944, 2008.

Jensen, M., Giangrande, S., Fairless, T., and Zhou, A.: Gridded Sonde VAP Product (GRIDDEDSONDE), Atmospheric Radiation Measurement (ARM) User Facility, https://doi.org/10.5439/1350631, 2024.

Jing, X. and Suzuki, K.: The impact of Process-Based warm rain constraints on the aerosol indirect effect, Geophysical Research Letters, 45, https://doi.org/10.1029/2018gl079956, 2018.

Kangaslahti, P., Lim, B., Gaier, T., Tanner, A., Varonen, M., Samoska, L., Brown, S., Lambrigtsen, B., Reising, S., Tanabe, J., Montes, O., Dawson, D., and Parashare, C.: Low noise amplifier receivers for millimeter wave atmospheric remote sensing, IEEE MTT-S International Microwave Symposium Digest, 1–3, https://doi.org/10.1109/mwsym.2012.6259468, 2012.

Khairoutdinov, M. F. and Randall, D. A.: Cloud resolving modeling of the ARM summer 1997 IOP: Model formulation, results, uncertainties, and sensitivities, J. Atmos. Sci., 60, 607–625, https://doi.org/10.1175/1520-0469(2003)060%3C0607:CRMOTA%3E2.0.CO;2, 2003.

Kurowski, M. J., Teixeira, J., Ao, C., Brown, S., Davis, A. B., Forster, L., Wang, K.-N., Lebsock, M., Morris, M., Payne, V., Richardson, M. T., Roy, R., Thompson, D. R., and Wilson, R. C.: Synthetic Observations of the Planetary Boundary Layer from Space: A Retrieval Observing System Simulation Experiment Framework, Bulletin of the American Meteorological Society, 104, E1999–E2022, https://doi.org/10.1175/bams-d-22-0129.1, 2023.

Kurowski, M.: Large eddy simulation of marine stratocumulus based on the VOCALS regional experiment [Data set]. Zenodo. https://doi.org/10.5281/zenodo.17078513, 2025.

Lamer, K., Oue, M., Battaglia, A., Roy, R. J., Cooper, K. B., Dhillon, R., and Kollias, P.: Multifrequency radar observations of clouds and precipitation including the G-band, Atmos. Meas. Tech., 14, 3615–3629, https://doi.org/10.5194/amt-14-3615-2021, 2021.

Lebsock, M. D. and L'Ecuyer, T. S.: The retrieval of warm rain from CloudSat, Journal of Geophysical Research Atmospheres, 116, https://doi.org/10.1029/2011jd016076, 2011.

https://doi.org/10.5194/egusphere-2025-4248
Preprint. Discussion started: 12 September 2025

Lhermitte, R.: Attenuation and scattering of millimeter wavelength radiation by clouds and precipitation, J. Atmos. Ocean. Tech., 7, 464–479, https://doi.org/10.1175/1520-0426(1990)007<464:AASOMW>2.0.CO;2, 1990.

Liu, Y., Geerts, B., Miller, M., Daum, P., and McGraw, R.: Threshold radar reflectivity for drizzling clouds, Geophysical Research Letters, 35, https://doi.org/10.1029/2007gl031201, 2008.

Löhnert, U., Crewell, S., and Simmer, C.: An integrated approach toward retrieving physically consistent profiles of temperature, humidity, and cloud liquid water. Journal of Applied Meteorology and Climatology, 43, 1295–1307, https://doi.org/10.1175/1520-0450(2004) 043<1295:AIATRP>2.0.CO;2, 2004.

Maahn, M., Turner, D. D., Löhnert, U., Posselt, D. J., Ebell, K., Mace, G. G., and Comstock, J. M.: Optimal estimation retrievals and their uncertainties: What every atmospheric scientist should know, Bulletin of the American Meteorological Society, 101, E1512–E1523, https://doi.org/10.1175/bams-d-19-0027.1, 2020.

Mace, G. G., Avey, S., Cooper, S., Lebsock, M., Tanelli, S., and Dobrowalski, G.: Retrieving co-occurring cloud and precipitation properties of warm marine boundary layer clouds with A-Train data, Journal of Geophysical Research Atmospheres, 121, 4008–4033, https://doi.org/10.1002/2015jd023681, 2016.

Mace, G., Marchand, R., Keywood, M., Protat, A., Humprhies, R., Fiddes, S., McCluskey, C., Siems, S., Huang, Y., May, P., and Ma, P-L.: Cloud and precipitation experiment at Kennaook (Cape-K) Science Plan, U.S. Department of Energy, Atmospheric Radiation Measurement user facility, 2023.

Meneghini, R., Bidwell, S. W., Liao, L., Rincon, R., and Heymsfield, G. M.: Differential-frequency Doppler weather radar: Theory and experiment, Radio Science, 38, https://doi.org/10.1029/2002rs002656, 2003.

Miles, N. L., Verlinde, J., and Clothiaux, E. E.: Cloud droplet size distributions in low-level stratiform clouds. Journal of the Atmospheric Sciences, 57(2), 295–311, 2000.

Morrison, H. and Gettelman, A.: A new Two-Moment Bulk Stratiform Cloud Microphysics Scheme in the Community Atmosphere Model, Version 3 (CAM3). Part I: Description and Numerical tests, Journal of Climate, 21, 3642–3659, https://doi.org/10.1175/2008jcli2105.1, 2008.

Mroz, K., Treserras, B. P., Battaglia, A., Kollias, P., Tatarevic, A., and Tridon, F.: Cloud and precipitation microphysical retrievals from the EarthCARE Cloud Profiling Radar: the C-CLD product, Atmospheric Measurement Techniques, 16, 2865–2888, https://doi.org/10.5194/amt-16-2865-2023, 2023.

Muhlbauer, A., McCoy, I. L., and Wood, R.: Climatology of stratocumulus cloud morphologies: microphysical properties and radiative effects, Atmos. Chem. Phys., 14, 6695–6716, https://doi.org/10.5194/acp-14-6695-2014, 2014.

Mülmenstädt, J., Salzmann, M., Kay, J. E., Zelinka, M. D., Ma, P.-L., Nam, C., Kretzschmar, J., Hörnig, S., and Quaas, J.: An underestimated negative cloud feedback from cloud lifetime changes, Nature Climate Change, 11, 508–513, https://doi.org/10.1038/s41558-021-01038-1, 2021.

O'Connor, E. J., Hogan, R. J., and Illingworth, A. J.: Retrieving stratocumulus drizzle parameters using doppler radar and LIDAR, Journal of Applied Meteorology, 44, 14–27, https://doi.org/10.1175/jam-2181.1, 2005.

https://doi.org/10.5194/egusphere-2025-4248
Preprint. Discussion started: 12 September 2025

O'Dell, C. W., Wentz, F. J., and Bennartz, R.: Cloud Liquid Water Path from Satellite-Based Passive Microwave Observations: A New Climatology over the Global Oceans, Journal of Climate, 21, 1721–1739, https://doi.org/10.1175/2007jcli1958.1, 2008.

Protat, A., Bouniol, D., Delanoë, J., O'Connor, E., May, P. T., Plana-Fattori, A., Hasson, A., Görsdorf, U., and Heymsfield, A. J.: Assessment of CloudSat reflectivity measurements and Ice cloud properties using Ground-Based and Airborne cloud radar observations, Journal of Atmospheric and Oceanic Technology, 26, 1717–1741, https://doi.org/10.1175/2009jtecha1246.1, 2009.

Rauber, R. M., Stevens, B., Ochs, H. T., Knight, C., Albrecht, B. A., Blyth, A. M., Fairall, C. W., Jensen, J. B., Lasher-Trapp, S. G., Mayol-Bracero, O. L., Vali, G., Anderson, J. R., Baker, B. A., Bandy, A. R., Burnet, E., Brenguier, J. -l., Brewer, W. A., Brown, P. R. A., Chuang, R., Cotton, W. R., Di Girolamo, L., Geerts, B., Gerber, H., Göke, S., Gomes, L., Heikes, B. G., Hudson, J. G., Kollias, P., Lawson, R. R., Krueger, S. K., Lenschow, D. H., Nuijens, L., O'Sullivan, D. W., Rilling, R. A., Rogers, D. C., Siebesma, A. P., Snodgrass, E., Stith, J. L., Thornton, D. C., Tucker, S., Twohy, C. H., and Zuidema, P.: Rain in shallow cumulus over the ocean: The RICO campaign, Bulletin of the American Meteorological Society, 88, 1912–1928, https://doi.org/10.1175/bams-88-12-1912, 2007.

Ray, P. S.: Broadband complex refractive indices of ice and water, Applied Optics, 11, 1836, https://doi.org/10.1364/ao.11.001836, 1972.

Rodgers, C. D.: Inverse Methods for Atmospheric Sounding: Theory and Practice. World Scientific, 240 pp., 2000.

Rosenkranz, P. W.: Water vapor microwave continuum absorption: A comparison of measurements and models, Radio Science, 33, 919–928, https://doi.org/10.1029/98rs01182, 1998.

Socuellamos, J. M., Monje, R. R., Cooper, K. B., Lebsock, M. D., Nagaraja, S. P. M., Siles, J. V., Beauchamp, R. M., and Tanelli, S.: A G-band doppler radar for atmospheric profiling, IEEE Transactions on Geoscience and Remote Sensing, 62, 1–8, https://doi.org/10.1109/tgrs.2024.3398616, 2024a.

Socuellamos, J. M., Monje, R. R., Lebsock, M. D., Cooper, K. B., and Kollias, P.: Dual-frequency (Ka-band and G-band) radar estimates of liquid water content profiles in shallow clouds, Atmospheric Measurement Techniques, 17, 6965–6981, https://doi.org/10.5194/amt-17-6965-2024, 2024b.

Socuellamos, J. M., Rodriguez Monje, R., Lebsock, M., and Cooper, K.: G-band radar observation during the CAPE-k campaign [Data set]. Zenodo. https://doi.org/10.5281/zenodo.17076276, 2025.

Soric, J., Kolias, N., Saunders, J., Kotce, J., Brown, A., Rodenbeck, C., and Gyurcsik, R. S.: A 100-W W-Band GAN SSPA, IEEE Microwave and Wireless Components Letters, 32, 712–715, https://doi.org/10.1109/lmwc.2022.3164710, 2022.

Stephens, G. L.: Remote Sensing of the Lower Atmosphere: An Introduction. Oxford University Press, 562 pp., 1994.

Stephens, G. L., Vane, D. G., Tanelli, S., Im, E., Durden, S., Rokey, M., Reinke, D., Partain, P., Mace, G. G., Austin, R., L'Ecuyer, T., Haynes, J., Lebsock, M., Suzuki, K., Waliser, D., Wu, D., Kay, J., Gettelman, A., Wang, Z., and Marchand, R.: CloudSat mission: Performance and early science after the first year of operation, Journal of Geophysical Research Atmospheres, 113, https://doi.org/10.1029/2008jd009982, 2008.

Straka, J. M.: Cloud and precipitation Microphysics: Principles and Parameterizations, Cambridge University Press, 2011.

https://doi.org/10.5194/egusphere-2025-4248
Preprint. Discussion started: 12 September 2025

Tansey, E., Marchand, R., Protat, A., Alexander, S. P., and Ding, S.: Southern Ocean Precipitation Characteristics Observed From CloudSat and Ground Instrumentation During the Macquarie Island Cloud & Radiation Experiment (MICRE): April 2016 to March 2017, Journal of Geophysical Research Atmospheres, 127, https://doi.org/10.1029/2021jd035370, 2022.

Trent, T., Schröder, M., and Remedios, J.: GEWEX Water Vapor Assessment: Validation of AIRS tropospheric humidity profiles with characterized radiosonde soundings, Journal of Geophysical Research Atmospheres, 124, 886–906, https://doi.org/10.1029/2018jd028930, 2019.

Wehr, T., Kubota, T., Tzeremes, G., Wallace, K., Nakatsuka, H., Ohno, Y., Koopman, R., Rusli, S., Kikuchi, M., Eisinger, M., Tanaka, T., Taga, M., Deghaye, P., Tomita, E., and Bernaerts, D.: The EarthCARE mission – science and system overview, Atmospheric Measurement Techniques, 16, 3581–3608, https://doi.org/10.5194/amt-16-3581-2023, 2023.

Wood, R., Mechoso, C. R., Bretherton, C. S., Weller, R. A., Huebert, B., Straneo, F., Albrecht, B. A., Coe, H., Allen, G., Vaughan, G., Daum, P., Fairall, C., Chand, D., Gallardo Klenner, L., Garreaud, R., Grados, C., Covert, D. S., Bates, T. S., Krejci, R., Russell, L. M., de Szoeke, S., Brewer, A., Yuter, S. E., Springston, S. R., Chaigneau, A., Toniazzo, T., Minnis, P., Palikonda, R., Abel, S. J., Brown, W. O. J., Williams, S., Fochesatto, J., Brioude, J., and Bower, K. N.: The VAMOS Ocean-Cloud-Atmosphere-Land Study Regional Experiment (VOCALS-REx): goals, platforms, and field operations, Atmos. Chem. Phys., 11, 627–654, https://doi.org/10.5194/acp-11-627-2011, 2011.

Yurk, N. Y., Lebsock, M., Socuellamos, J., Monje, R. R., Cooper, K., and Kollias, P.: Vertical Wind and Drop Size Distribution Retrieval with the CloudCube G-band Doppler Radar, Atmospheric Measurement Techniques, https://doi.org/10.5194/egusphere-2025-618, 2025.

Zhang, M., Liu, X., Diao, M., D'Alessandro, J. J., Wang, Y., Wu, C., Zhang, D., Wang, Z., and Xie, S.: Impacts of Representing Heterogeneous Distribution of Cloud Liquid and Ice on Phase Partitioning of Arctic Mixed-Phase Clouds with NCAR CAM5, Journal of Geophysical Research Atmospheres, 124, 13071–13090, https://doi.org/10.1029/2019jd030502, 2019.

Zhu, Z., Kollias, P., Luke, E., and Yang, F.: New insights on the prevalence of drizzle in marine stratocumulus clouds based on a machine learning algorithm applied to radar Doppler spectra, Atmospheric Chemistry and Physics, 22, 7405–7416, https://doi.org/10.5194/acp-22-7405-2022, 2022.